PHYSICAL REVIEW B **106**, 235308 (2022)

# Tunable polarized terahertz wave generation induced by spontaneous polarization-dependent ultrafast shift current from vertically grown ferroelectric SnS

Jing Wang,[1] Yuanyuan Huang,[1,*] Zhen Lei,[1] Yayan Xi,[1] Wanyi Du,[1] Xueqin Cao,[1] Yanqing Ge,[1]
Lipeng Zhu,[1,2] Yixuan Zhou,[1] and Xinlong Xu[1,†]
[1] *Shaanxi Joint Lab of Graphene, State Key Laboratory of Photon-Technology in Western China Energy,*
*International Collaborative Center on Photoelectric Technology and Nano Functional Materials,*
*Institute of Photonics & Photon-Technology, Northwest University, Xi'an 710069, China*
[2] *School of Electronic Engineering, Xi'an University of Posts and Telecommunications, Xi'an 710121, China*

(Received 28 July 2022; revised 21 September 2022; accepted 24 October 2022; published 8 December 2022)

Ferroelectric group-IV monochalcogenides $MX$ ($M$ = Sn/Ge and $X$ = S/Se) are of particular importance for the new-generation photovoltaic devices due to their special in-plane spontaneous polarization resulting in a bulk photovoltaic effect. However, the spontaneous polarization and its related dynamical photoresponse under an ultrafast laser excitation are rarely studied via a noncontact all-optical method. Herein, the vertically grown SnS nanosheets have been synthesized by a physical vapor deposition (PVD) method and the corresponding spontaneous polarization is characterized via the terahertz (THz) emission spectroscopy. The primary THz emission mechanism is ascribed to the shift current, which is proved by the THz wave dependences on the pump light polarization angle and pump fluence. Interestingly, the shift current depends on the spontaneous polarization along the SnS nanosheet grown direction, according to the reversed polarity of the THz wave under opposite directional excitations. Furthermore, the amplitude and phase of the THz wave are modulated by the pump light polarization angle, resulting in the elliptical THz wave emission with tunable ellipticity and orientation angle. Our study has shed light on the shift current of ferroelectrics and controllable polarized THz wave generation, which provides application prospects for ferroelectric-based photovoltaics, nonlinear photonics, and THz polarized devices.

DOI: 10.1103/PhysRevB.106.235308

## I. INTRODUCTION

Shift current has attracted extensive interest as the primary physical origin of the bulk photovoltaic effect, due to its unique potential to surpass the Shockley-Queisser limit in photovoltaic applications [1,2]. Unlike the traditional photocurrent generation in *p-n* junctions, shift current is generated by the coherent evolution of electron and hole wave functions in noncentrosymmetric materials under light illumination [3,4]. Intriguingly, the ferroelectrics have inherent inversion asymmetry [5], switchable polarization direction [6], and large carrier mobility [7–9], which make them more suitable for photovoltaic applications than some traditional bulk semiconductors. In particular, the ferroelectricity-induced internal in-plane electric field can accelerate the separation of the photogenerated carriers to form a robust shift current [10]. Therefore, these intrinsic properties enable ferroelectrics to be promising material selections for photovoltaic applications.

Among the ferroelectrics, the orthorhombic group-IV monochalcogenide materials $MX$ ($M = \mathrm{Sn/Ge}$ and $X = \mathrm{S/Se}$) [6,10–12] exhibit intriguing potentials in optoelectronic devices such as memory devices [10] and solar cells [13] due to the strongly coupled ferroelectricity and ferroelasticity at room temperature. As a typical $MX$, SnS is expected to be an ideal candidate for photovoltaic devices from three aspects. First, SnS has better chemical stability than Ge$X$ [14], and the Curie temperature of ferroelectric phase transition in SnS (1200 K) is much higher than that of SnSe (326 K) [6], indicating the ferroelectric stability of SnS. Second, SnS has a wide band gap (0.3–1.8 eV according to the material phase) [15–17], high carrier mobility (tens of thousands of $\mathrm{cm}^2\ \mathrm{V}^{-1}\ \mathrm{s}^{-1}$) [18], and strong optical absorption ($>10^4\ \mathrm{cm}^{-1}$) [18], suggesting the ability of highly efficient light to current conversion. Last but not least, the large in-plane spontaneous polarization ($\sim 2.62 \times 10^{-10}$ C/m) of SnS [6,11,14,19] is introduced by the puckered structures of atomic arrangements [12], which is well correlated to the shift current generation. As expected, the first-principles calculations indicate that SnS has a significant shift current, up to 100 $\mu\mathrm{A/V}^2$ [7]. However, the experimental evidence of the shift current induced by spontaneous polarization from SnS is still insufficient up to now, which calls for an efficient and sensitive way to study the shift current in ferroelectrics.

Previously, the photovoltaic response in ferroelectrics was experimentally detected by the photocurrent measurement with the requirement of external electrode fabrication onto the sample [20,21]. However, this method may cause parasite effects from the impurities and interface contact, which unfortunately reduces the light to current conversion efficiency and slows down the photoresponse [1]. Therefore, all-optical

---

[*] yyhuang@nwu.edu.cn
[†] xlxuphy@nwu.edu.cn

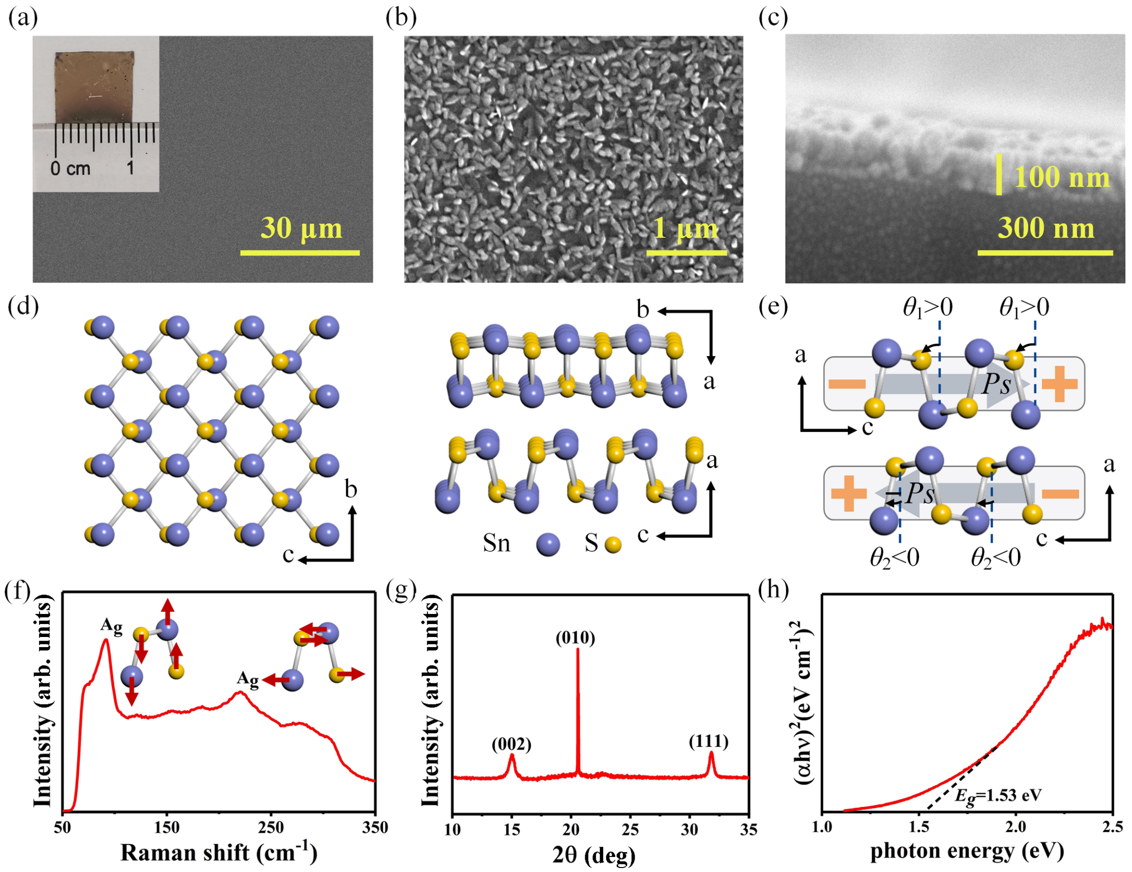

FIG. 1. (a)–(c) The photograph, the top-view, and side-view SEM images of VG SnS. (d) The atomic structure of SnS from the top and side views. (e) The spontaneous polarization $P_S$ within the SnS film. (f) Raman spectrum of the VG SnS, of which the vibrational $A_g$ modes are depicted in the inset. (g) XRD spectrum of the VG SnS. (h) UV-Vis spectrum of the VG SnS.

spectroscopy becomes a better approach because of the efficient excitation and collection of the photocurrent [1,22]. Terahertz (THz) emission spectroscopy is a reliable method with high sensitivity and nondestructive detection, which establishes a link between macroscopic information and microscopic physical origins. When ferroelectrics are impinged by the femtosecond (fs) laser, the microscopic optical physics such as optical transition, electron density of states, spin-orbit coupling, and electron-hole separation determine the carrier distribution, built-in electric field, nonlinear optical process [23–25], and so forth. These physical properties can be revealed via the macroscopic amplitude, phase, polarity, and polarization information of the generated THz wave [26,27], such as various surface states-involved optical transitions in $Bi_2Se_3$ [28] and the asymmetric distribution of densities of states and charge displacement in GaTe [29]. Besides, Kushnir *et al.* have observed the shift current that is determined by the spontaneous polarization in ferroelectric semiconductors GeSe [30] and GeS [31] from their THz emission. However, the shift current vanishes along mirror symmetric directions in monolayer $MX$s [7,22], which may restrict its photovoltaic response along some certain directions. In addition, there have been few reports of the THz wave emission and the shift current induced by spontaneous polarization from SnS. How to generate, manipulate, and probe the spontaneous polarization-induced shift current via the THz emission spectroscopy is an important issue for photovoltaic applications.

In this work, in order to address these critical issues, we have prepared the vertically grown SnS (VG SnS) to enhance the light-matter interaction due to the arrays of SnS nanosheets and increased absorption of incident photons compared with the single-layer SnS. Then the THz wave is generated from the VG SnS under the femtosecond (fs) excitation, which is dominated by the shift current according to the THz wave dependences on the pump light polarization angle and the pump fluence. In particular, the THz wave polarity depends directly on the incident plane direction, indicating the dominant role of the net spontaneous polarization along the SnS grown direction. These results elucidate the physics between microscopic spontaneous polarization and macroscopic THz emission properties, which supplements the study of ferroelectric-based shift current in the THz regime.

## II. CHARACTERIZATION AND EXPERIMENTAL SETUP

The VG SnS thin film with a size of ∼1 × 1 $cm^2$ was synthesized on a sapphire substrate by a physical vapor deposition (PVD) method [32] as presented in the inset of Fig. 1(a). The disordered SnS nanosheets with vimineous structures grow vertically with respect to the substrate [Figs. 1(a)–1(c)], which is characterized by SEM (scanning electron microscope, Thermo Scientific, Apreo S., U.S.A.). The thickness of VG SnS film is ∼100 nm according to the scale of the side-view SEM image [Fig. 1(c)]. As the 100 nm thick SnS film

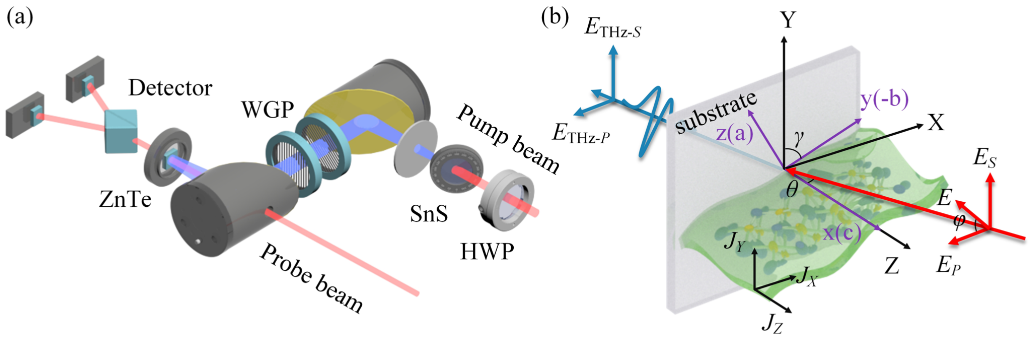

FIG. 2. (a) The schematic of the experimental setup of the THz emission spectroscopy in a transmission configuration. (b) The THz wave is generated by the transient photocurrent $J$ within VG SnS nanosheets. The laboratory coordinate is represented by $(XYZ)$, while the crystalline coordinate of VG SnS is represented via $(xyz)$. The $a$, $b$, and $c$ axes represent the crystalline axes of the SnS. The incident angle $\theta$ is defined as the angle between the normal direction of the substrate and the incident light. The polarization angle and the azimuthal angle are labeled by $\varphi$ and $\gamma$, respectively.

is very densely populated (with numerous SnS nanosheets), it can emit a stronger THz wave than that from a single-layer SnS (0.58 nm thick) [14]. As shown in Fig. 1(d), the atomic structure of SnS is analogous to black phosphorus [33,34]. Sn and S atoms are connected by covalent bonds, which exhibit an orthorhombic array within the *b*-*c* plane from the top view [35]. The side view possessing a single-layer structure shows a zigzag arrangement within the *a*-*b* plane and an armchair arrangement within the *a*-*c* plane [36], where the individual layers are maintained together by the van der Waals interaction [15]. Interestingly, the first-principles calculations have proved the tilting angles ($\theta_1$ and $\theta_2$) between Sn and S atoms determine the amplitude and polarity of spontaneous electric polarization ($P_S$) and ferroelectricity [6,12]. As illustrated in Fig. 1(e), the tilting angles are positive (negative) when the S (Sn) atom is anterior to the Sn (S) atom. The spontaneous polarization only appears when the tilting angles are nonzero, and the polarization direction is reversed from $P_S$ to $-P_S$ after reversing the tilting angles [19]. Therefore, the spontaneous polarization amplitude increases proportionally with the tilting angle [6,7], which further determines the integral shift current tensor and could also influence the THz emission spectroscopy. The vibration modes and the orthorhombic phase of SnS are characterized by the SmartRaman confocal-micro-Raman module (Institute of Semiconductors, Chinese Academy of Science) with a 532 nm laser excitation, as shown in Fig. 1(f). The peaks at 92.4 and 221 $\text{cm}^{-1}$ originate from the $A_g$ mode with the "waving" type longitudinal vibration and the "NaCl" type transverse vibration [37,38], respectively. According to the surface and cross-sectional morphology features, the Raman peaks are directly related to the orientation angle (the angle between the vertically grown SnS layer and substrate) of the SnS layer [39]. With the increase of the orientation angle, the Raman peaks are weakened in the range of 150–210 $\text{cm}^{-1}$. When the orientation angle is ~90°, there are two obvious $A_g$ modes in the Raman spectrum, which are in accord with our results in Fig. 1(f). The lattice structure is also confirmed by x-ray diffraction (XRD) (Bruker, D8 Advance) as depicted in Fig. 1(g), where the XRD peaks at 15.1°, 20.6°, and 31.8° correspond to the (002), (010), and (111) lattice planes (JCPDS #53-0526) [39]. In order to further investigate the optical properties of the VG SnS film, the absorption spectrum is carried out via UV-Vis spectroscopy (R1, Ideaoptics). Figure 1(h) shows that the absorption increases with the photon energy from 1.0 to 2.5 eV. In addiiton, the band gap energy of the VG SnS is estimated as 1.53 eV based on the absorption spectrum of the Tauc plot by the formula $(\alpha h\nu)^2 = A(h\nu - E_g)$, where $A$ is a proportionality constant, $h$ is Planck's constant, $\nu$ is the frequency of excitation light, $E_g$ is the optical band gap, and $\alpha$ is the absorption coefficient [40].

The THz emission spectroscopy with transmission configuration is employed to characterize the VG SnS as shown in Fig. 2(a). A Ti:sapphire regenerative amplifier (Spitfire Ace, Spectra-Physics) is utilized to pump the VG SnS with an 800 nm central wavelength. Then the pump light with ~3 mm diameter impinges on the sample to emit THz waves, and the probe beam detects the generated THz signal in the time domain [41]. Along the pump light path, a half-wave plate (HWP) and a polyethylene plate are placed before and behind the sample to vary the polarization state of the incident laser and filter out the transmitted infrared light, respectively. The emitted THz wave is collected by the off-axis parabolic mirrors and overlaps with the probe light on the detection ZnTe crystal.

In order to study the optical response of the VG SnS under the fs illumination, the Cartesian coordinate system is supposed to be established considering the crystallographic system of the VG SnS [42]. As presented in Fig. 2(b), the crystalline coordinate of VG SnS nanosheets is defined as $(xyz)$. The $z$ axis is chosen along the normal direction of the VG SnS nanosheets, while the $x$ and $y$ axes are within the nanosheet plane. Herein, the SnS nanosheets are grown vertically on the substrate. In order to set the $z$ direction perpendicular to the basal plane of the SnS, the $z$ axis is set parallel to the substrate as shown in Fig. 2(b). In the laboratory coordinate $(XYZ)$, the incident light is tuned between *p*- ($E_P$) and *s*-polarization ($E_S$) states after rotating the polarization angle $\varphi$ by the HWP. The azimuthal angle $\gamma$, as a manifestation of the sample orientation, is introduced to represent the angle between the laboratory and crystalline coordinates. This angle is varied via rotating the VG SnS plane with respect to the normal direction of the substrate ($Z$ axis). Finally, the horizontal ($E_{\text{THz-}P}$) and vertical ($E_{\text{THz-}S}$) components of the generated THz pulses are detected via wire-grid polarizers (WGPs) [43]. In general, the

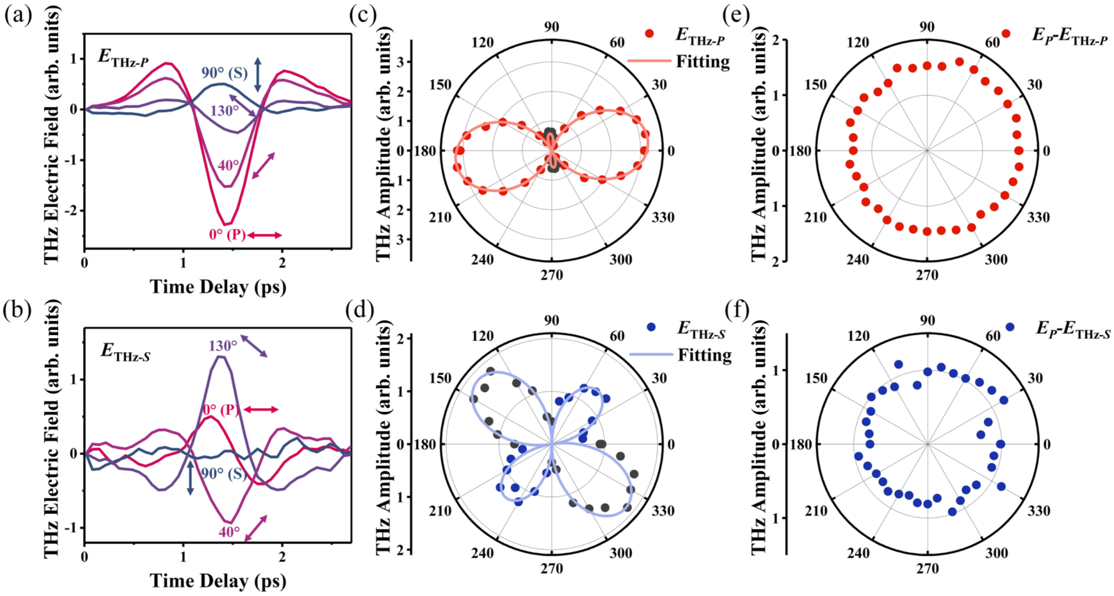

FIG. 3. (a) $E_{\mathrm{THz}\text{-}P}$ and (b) $E_{\mathrm{THz}\text{-}S}$ components of generated THz electric field from VG SnS with the pump light polarization angle of 0° ($E_P$), 40°, 90° ($E_S$), and 130°. The arrows represent the polarization states of the pump light. THz peak to valley amplitude of the (c) $E_{\mathrm{THz}\text{-}P}$ and (d) $E_{\mathrm{THz}\text{-}S}$ with respect to the pump light polarization angle in polar coordinates. The solid lines represent the fitting results from Eq. (3). THz peak to valley amplitude of the (e) $E_P$-$E_{\mathrm{THz}\text{-}P}$ and (f) $E_P$-$E_{\mathrm{THz}\text{-}S}$ with various azimuthal angles in polar diagrams.

generated THz radiation is induced by the transient photocurrent $J$ or nonlinear polarization $P$ as $E_{\mathrm{THz}} \propto \partial P^2/\partial t^2 + \partial J/\partial t$ [24]. The nonlinear polarization $P$ can be excluded since the real carriers are generated under the above band gap excitation (800 nm @ 1.55 eV), which results in the transient photocurrent response rather than nonresonant nonlinear polarization [44]. Therefore, we consider the photocurrent $J$ contribution to the THz radiation of the VG SnS only. Based on the coordinates in Fig. 7 (in Appendix A), the THz electric field components are written as $E_{\mathrm{THz}\text{-}P} \propto -\cos\theta_{\mathrm{THz}}(\partial J_X/\partial t) + \sin\theta_{\mathrm{THz}}(\partial J_Z/\partial t)$ and $E_{\mathrm{THz}\text{-}S} \propto \partial J_Y/\partial t$ according to the dipole radiation theory [45], and the $\theta_{\mathrm{THz}}$ represents the refraction angle of the emitted THz wave inside VG SnS.

## III. RESULTS AND DISCUSSION

### A. Angular dependence of the emitted THz wave

When the 800 nm fs laser impinges on the VG SnS with a 45° incident angle and 0.71 $\mathrm{mJ/cm^2}$ pump fluence, the $E_{\mathrm{THz}\text{-}P}$ and $E_{\mathrm{THz}\text{-}S}$ components of the generated THz wave under different polarization state illuminations are depicted in Figs. 3(a) and 3(b), respectively. Both the $E_{\mathrm{THz}\text{-}P}$ and $E_{\mathrm{THz}\text{-}S}$ components of the time-domain THz signals present an approximate 3 ps time duration and directly depend on the incident polarization state. For the $E_{\mathrm{THz}\text{-}P}$ component, the THz waveform polarities are opposite when the VG SnS is excited under $E_P(\varphi = 0^\circ)$ and $E_S(\varphi = 90^\circ)$ fs laser excitations, and the maximum THz amplitude appears at $E_P$ excitation. Unlike the $E_{\mathrm{THz}\text{-}P}$ component, the $E_{\mathrm{THz}\text{-}S}$ component presents an amplitude maximum when $\varphi = 130^\circ$, and the THz radiation is almost vanishing under the $E_S$ illumination. In order to further investigate the differences between the THz components, the peak to valley values of $E_{\mathrm{THz}\text{-}P}$ and $E_{\mathrm{THz}\text{-}S}$ components with respect to the pump light polarization angle $\varphi$ are portrayed in Figs. 3(c) and 3(d). Herein, the black dots with positive values indicate the THz valley-peak-valley waveforms (such as the $E_{\mathrm{THz}\text{-}S}$ component under the excitation of $\varphi = 130^\circ$), while the red or blue dots with negative values represent the THz peak-valley-peak waveforms (such as the $E_{\mathrm{THz}\text{-}P}$ component under the $E_p$ excitation). It can be seen that both the $E_{\mathrm{THz}\text{-}P}$ and $E_{\mathrm{THz}\text{-}S}$ components exhibit twofold rotational symmetry with the pump light polarization angle $\varphi$ in the polar plots. However, the petal sizes of two THz components have distinct differences. The blue petal is slightly smaller than the black petal for the $E_{\mathrm{THz}\text{-}S}$ component [Fig. 3(d)], while the red petal is much larger than the black petal for the $E_{\mathrm{THz}\text{-}P}$ component [Fig. 3(c)], which indicates a significant offset of the THz amplitude towards the negative direction in the $E_{\mathrm{THz}\text{-}P}$ component. This difference mainly comes from the photocurrent distributions as $J_X$ and $J_Z$ concurrently contribute to the $E_{\mathrm{THz}\text{-}P}$ component, and only $J_Y$ contributes to the $E_{\mathrm{THz}\text{-}S}$ component based on the coordinates in Fig. 2(b). Due to the VG SnS nanosheets, the photocurrent $J_Z$ plays an important role in the $E_{\mathrm{THz}\text{-}P}$ component, which exhibits a distinguishing THz radiation property from the $E_{\mathrm{THz}\text{-}S}$ component.

Aside from the extrinsic polarization state, the intrinsic surface homogeneity of the VG SnS nanosheets can also influence the carrier drift, diffusion, and charge center shift, which further determine the photocurrent response as well as the THz emission spectroscopy. This is studied by the $E_{\mathrm{THz}\text{-}P}$ and $E_{\mathrm{THz}\text{-}S}$ components' evolution as the azimuthal angle $\gamma$ of the VG SnS at the fixed $E_p$ excitation is rotated. As shown in Figs. 3(e) and 3(f), the peak to valley values of both THz components present circular dependences on the azimuthal angle $\gamma$ in polar diagrams, which suggests the VG SnS nanosheets exhibit an isotropic photocurrent response within the VG SnS plane (parallel to the substrate plane). This is different from the azimuthal angle sensitive THz radiation that generally

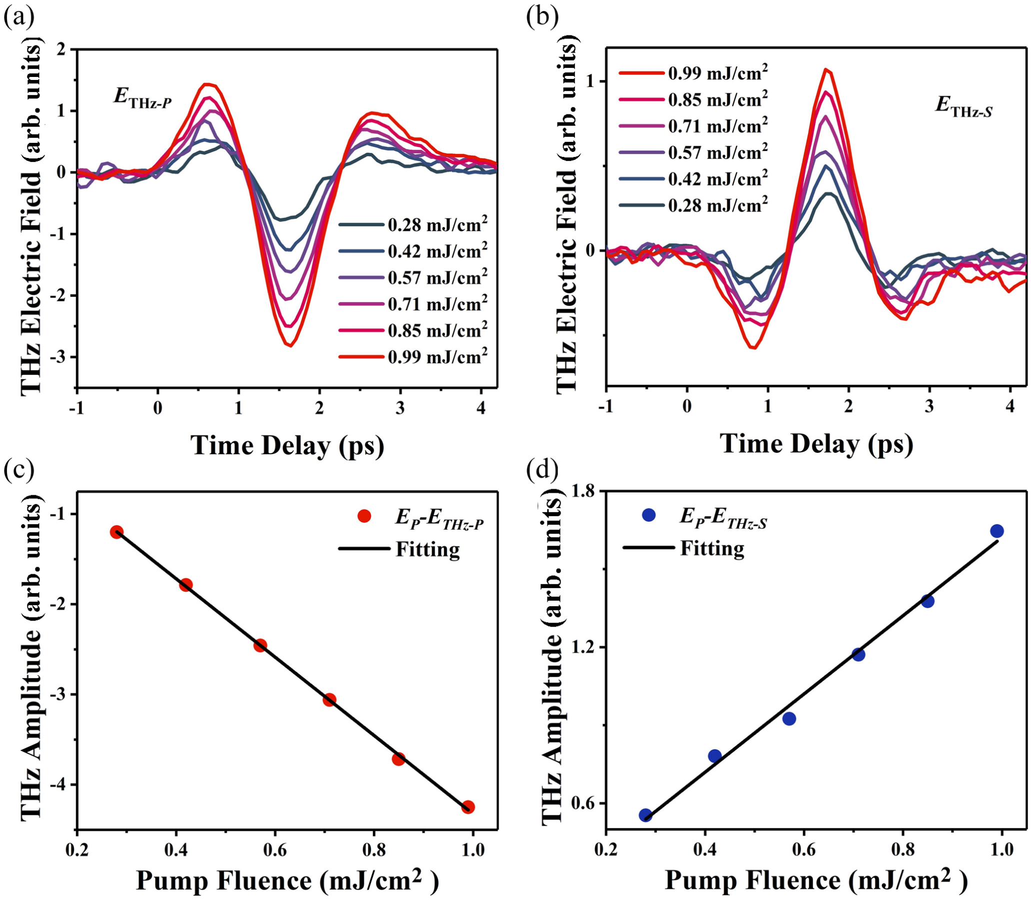

FIG. 4. Comparison of the pump fluence dependent (a) $E_{\text{THz-}P}$ and (b) $E_{\text{THz-}S}$ components under $E_P$ excitation and the extracted peak to valley values of (c) $E_{\text{THz-}P}$ and (d) $E_{\text{THz-}S}$ components. The dotted and solid lines represent experimental and linear fitting results, respectively.

occurs on three kinds of materials. The first one is the natural crystal with explicit surface rotational symmetry such as InAs [46], $MoS_2$ [43], and $SnS_2$ [25], of which the azimuthal angle is directly related to the nonlinear susceptibility and influences the THz radiation properties. The second one is induced by the asymmetric built-in field such as the thermoelectric field that is associated with the thermal diffusion current (Seebeck effect) in thermoelectric materials [47], electric potentials because of breaking conduction paths in graphite [48], and the acceleration field of carriers along a preferred direction due to the stacking faults in aligned carbon nanotubes [49]. The third one is the material with in-plane anisotropy such as $WSe_2$ [27] and $PdSe_2$ [50], which generate the asymmetric THz radiation along a preferred photocurrent direction or puckered direction of atomic bonds. As for the prepared sample, the VG SnS nanosheets are grown randomly on the substrate [Fig. 1(b)], which minimizes the preferred orientation of the photocurrent and results in the isotropic THz radiation with respect to the azimuthal angle $\gamma$. This isotropic distribution of the THz radiation has been observed in the vertically grown graphene with a random arrangement of nanosheets as well [23]. Moreover, the uniformity of THz wave generation at different areas of the VG SnS sample is satisfactory. We have measured the THz emission after moving the sample along transversal and longitudinal directions with a step of 0.25 mm. The amplitude, phase, and polarity of the emitted THz waves are almost identical at different areas of the sample.

### B. Pump fluence dependence of the emitted THz wave

The dependences of $E_{\text{THz-}P}$ and $E_{\text{THz-}S}$ components on the pump fluence are presented in Fig. 4. Herein, the positive and negative THz amplitude values represent opposite THz waveform polarities, and the incident light is fixed at the $E_P$ state. With the pump fluence ranging from 0.28 to 0.99 $\text{mJ/cm}^2$, the THz amplitude of both $E_{\text{THz-}P}$ and $E_{\text{THz-}S}$ components increase continuously as shown in Figs. 4(a) and 4(b), respectively. It is noteworthy that the peak to valley values of the emitted THz wave with respect to the pump fluence are well fitted by linear functions for both components, as shown in Figs. 4(c) and 4(d). This indicates that the THz emission from VG SnS is dominated by the second-order nonlinear effect [51] due to the linear relationship between the pump fluence and THz amplitude as $E_{\text{THz}} \propto \chi^{(2)}|E_{(\omega)}|^2 \propto I$ [43,52], where $I$ is the intensity of pump light.

The second-order nonlinear effect that generates transient photocurrent includes the linear photogalvanic effect (LPGE) [53], circular photogalvanic effect (CPGE) [54], linear photon drag effect (LPDE) [23], and circular photon drag effect (CPDE) [55]. In this work, the pump light is linearly polarized, which excludes the CPGE and CPDE as they are generally induced under circularly polarized excitation. The LPGE is also cognized as the shift current, which arises from a spatial displacement of electron density along the atomic bonds or emerges as a result of asymmetric relaxation of

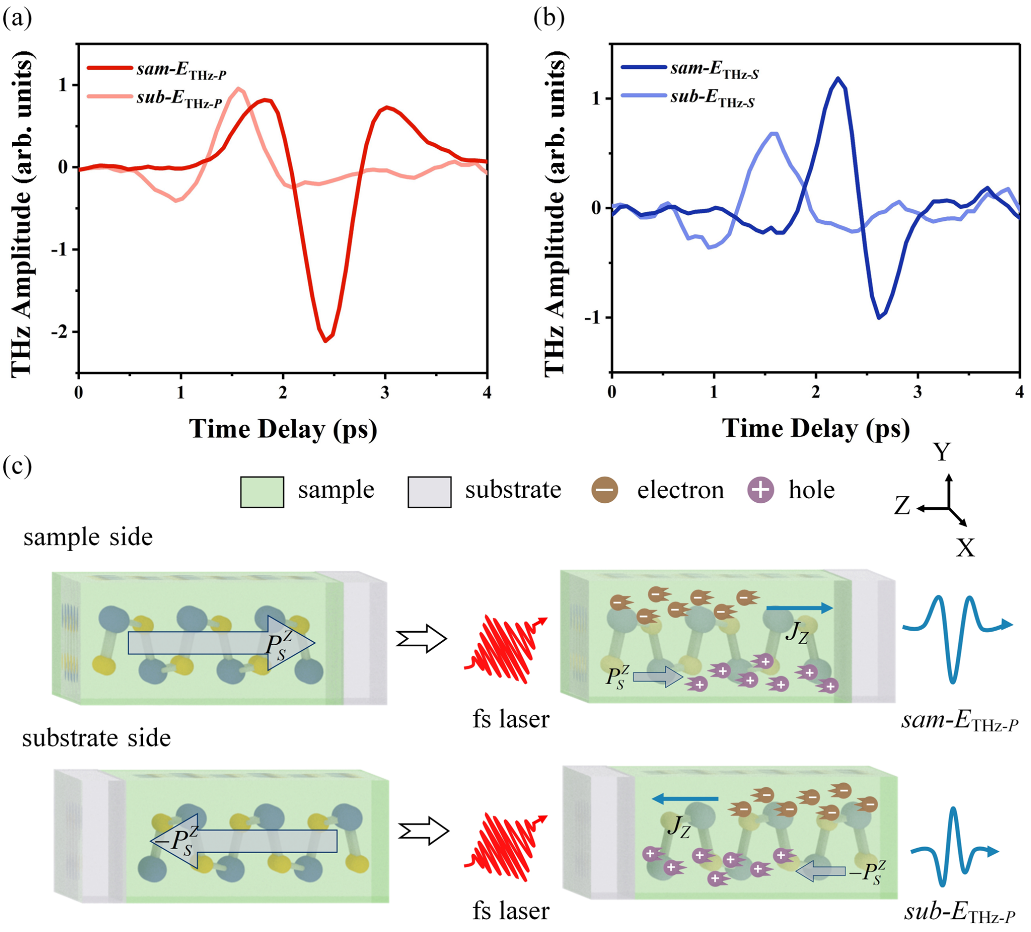

FIG. 5. (a), (b) The comparison of $E_{\text{THz-}P}$ and $E_{\text{THz-}S}$ components under the *sub*- and *sam*-side plane excitations. (c) The schematical exciting process of photocurrent $J_Z$ and generated THz emission of the VG SnS under opposite directional excitations.

excited electrons or holes [28,53]. To obtain a net current in the direction of the bonds, the LPGE can only occur in the materials with broken inversion symmetry [22,53]. On the contrary, the LPDE is not limited by the inversion symmetry of materials since it comes from the momentum transfer from incident photons to carriers. This momentum transfer process is supported by lattice vibration and electron-phonon coupling [56], and then the photon drag current is generated during the momentum relaxation time. The photon drag current is sensitive to the photon wave vector $\boldsymbol{k}$ due to the momentum transfer [53], which will reverse the photocurrent direction as well as the generated THz waveform polarity after tuning $\boldsymbol{k}$ into $-\boldsymbol{k}$.

### C. Incident plane dependence of the emitted THz wave

In order to clarify the THz emission mechanism between the LPGE and LPDE, we compare the THz wave excited from the sample side (*sam*-$E_{\text{THz-}P}$ and *sam*-$E_{\text{THz-}S}$) and the substrate side (*sub*-$E_{\text{THz-}P}$ and *sub*-$E_{\text{THz-}S}$), which is equivalent to reversing the incident wave vector $\boldsymbol{k}$. As shown in Figs. 5(a) and 5(b), the THz amplitude under the sample-side excitation is larger than that under the substrate-side excitation for both $E_{\text{THz-}P}$ and $E_{\text{THz-}S}$ components. However, the THz waveforms of the $E_{\text{THz-}P}$ component have opposite polarities under opposite incident planes, while the $E_{\text{THz-}S}$ component has identical THz waveform polarities under opposite incident planes. Obviously, the wave-vector dependence does not occur in the $E_{\text{THz-}S}$ component, which does not satisfy the essential property of the LPDE [23]. Therefore, the contribution of LPDE is not involved and the LPGE is the primary mechanism for the THz emission in the VG SnS.

The different wave-vector dependences of the THz components are directly related to the photocurrent components according to the coordinates in Fig. 2(b). The $E_{\text{THz-}P}$ component is determined by the $J_X$ and $J_Z$ as $E_{\text{THz-}P} \propto -\cos\theta_{\text{THz}}(\partial J_X/\partial t) + \sin\theta_{\text{THz}}(\partial J_Z/\partial t)$, and the $E_{\text{THz-}S}$ component is influenced by the $J_Y$ only. After reversing the incident plane, the $E_{\text{THz-}S}$ component keeps the same direction, while the $E_{\text{THz-}P}$ component is changed to $E_{\text{THz-}P} \propto -\cos\theta_{\text{THz}}(\partial J_X/\partial t) - \sin\theta_{\text{THz}}(\partial J_Z/\partial t)$. This is caused by the reversed $J_Z$ from opposite excitation sides in the VG SnS as shown in Fig. 5(c). According to the atomic structure of SnS, the spontaneous polarization $P_S$ is formed along the S-Sn bonds as shown in Fig. 1(e). Due to the lone pair electrons in the Sn atoms and large electronic coupling between adjacent layers [14,57,58], the VG SnS nanosheets were synthesized on the substrate starting from the Sn atoms, which further introduce the preferred AA stacking order. Then the identical ferroelectricity and a net polarization $P_S^Z$ are induced along the $Z$ axis. Under the action of the spontaneous polarization $P_S^Z$, the separation and acceleration of electrons and holes within the VG SnS are enhanced to form a large shift current after being excited by the fs laser [7,10,31]. The electric field induced by the shift current is also parallel to the atomic layer, which satisfies the definition of the in-plane electric field; then the VG SnS do not influence the dimensionality of the ferroelectric-induced electric field [59]. Thus, the shift current directly depends on the spontaneous polarization orientation. $P_S^Z$ changes to $-P_S^Z$ after reversing the incident plane, resulting in the photocurrent reversal of $J_Z$ [60–62], while $J_X$ and $J_Y$ have identical directions excited from opposite incident planes. Therefore, only the $E_{\text{THz-}P}$ component containing the $J_Z$ contribution presents polarity reversal under the opposite directional excitations. In this scenario, the internal manipulation of spontaneous polarization is realized without an external bias voltage, indicating the potential of VG SnS as a candidate for next-generation photovoltaic devices.

### D. Physical description of the shift current

As proof of LPGE for the THz emission, the phenomenal description of the LPGE-induced shift current is given by [63]

$$J_\lambda^{\text{PGE}} = \sigma_{\lambda\mu\upsilon}^{l}\frac{E_\mu E_\upsilon^* + E_\upsilon E_\mu^*}{2}, \tag{1}$$

where $\sigma_{\lambda\mu\upsilon}^{l}$ is the third-rank tensor of the nonlinear conductivity and $E_{\mu,\upsilon}$ represents the incident electric field. According to the coordinate systems of VG SnS nanosheets as shown in Fig. 2(b), the shift current components are given as follows (see detailed calculation in Appendix B):

$$\begin{aligned}
J_X ={}& (\sigma_{yyz}+\sigma_{yzy})CE^2\left(\frac{1}{4}C\cos^2\varphi - \frac{1}{2}C\sin^2\varphi\right)I - \frac{1}{2}CE^2\sigma_{zxx}\cos^2\varphi I - \sigma_{zyy}CE^2\left(\frac{1}{2}\pi\cos^2\varphi + \pi\sin^2\varphi + \frac{\sqrt{2}}{4}C\sin 2\varphi\right)I\\
&- \sigma_{zzz}CE^2\left(\frac{1}{2}\pi\cos^2\varphi + \pi\sin^2\varphi - \frac{\sqrt{2}}{4}C\sin 2\varphi\right)I,\\
J_Y ={}& (\sigma_{yyz}+\sigma_{yzy})CE^2\left(\frac{1}{4}C\cos^2\varphi - \frac{1}{2}C\sin^2\varphi\right)I + \frac{1}{2}CE^2\sigma_{zxx}\cos^2\varphi I + \sigma_{zyy}CE^2\left(\frac{1}{2}\pi\cos^2\varphi + \pi\sin^2\varphi + \frac{\sqrt{2}}{4}C\sin 2\varphi\right)I\\
&+ \sigma_{zzz}CE^2\left(\frac{1}{2}\pi\cos^2\varphi + \pi\sin^2\varphi - \frac{\sqrt{2}}{4}C\sin 2\varphi\right)I,\\
J_Z ={}& (\sigma_{xzx}+\sigma_{xxz})E^2\left(\frac{1}{2}C\cos^2\varphi - \frac{\sqrt{2}}{4}C\sin 2\varphi\right)I.
\end{aligned} \tag{2}$$

Herein, the shift current components $J_X$ and $J_Y$ are parallel to the substrate ($XY$-plane direction) according to Fig. 2(b). The incident angle is 45° and the azimuthal angle $\gamma$ is integrated from 0 to $2\pi$ due to the random arrangement of the VG SnS nanosheets. The coefficient $C$ represents the integral result. Then the THz electric field components of the VG SnS are described as

$$E_{\text{THz-}P} \propto A_X\cos^2\varphi + B_X\sin^2\varphi + C_X\sin 2\varphi + S_X,\quad E_{\text{THz-}S} \propto A_Y\cos^2\varphi + B_Y\sin^2\varphi + C_Y\sin 2\varphi + S_Y. \tag{3}$$

The constant terms $S_X$ and $S_Y$ represent polarization-independent background current [64]. The fitting coefficients are related to the nonlinear conductivity tensor elements of the VG SnS shown as follows:

$$\begin{aligned}
A_X ={}& -\frac{1}{4}C^2(\sigma_{yyz}+\sigma_{yzy})\cos\theta_{\text{THz}} + \frac{1}{2}C\sigma_{zxx}\cos\theta_{THz}\\
&+ \frac{1}{2}\pi\sigma_{zyy}C\cos\theta_{\text{THz}} + \frac{1}{2}\pi\sigma_{zzz}C\cos\theta_{\text{THz}}\\
&+ \frac{1}{2}C\sin\theta_{\text{THz}}(\sigma_{xzx}+\sigma_{xxz}),\\
B_X ={}& \frac{\sqrt{2}}{4}C^2\sigma_{zyy}\cos\theta_{\text{THz}} - \frac{\sqrt{2}}{4}C^2\sigma_{zzz}\cos\theta_{\text{THz}}\\
&- \frac{\sqrt{2}}{4}C(\sigma_{xzx}+\sigma_{xxz})\sin\theta_{\text{THz}},\\
C_X ={}& \cos\theta_{\text{THz}}C\left[\frac{1}{2}(\sigma_{yyz}+\sigma_{yzy})C + \pi(\sigma_{zyy}+\sigma_{zzz})\right],\\
A_Y ={}& \frac{1}{4}(\sigma_{yyz}+\sigma_{yzy})C^2 + \frac{1}{2}C\sigma_{zxx} + \frac{1}{2}\pi C(\sigma_{zyy}+\sigma_{zzz}),\\
B_Y ={}& \frac{\sqrt{2}}{4}C^2(\sigma_{zyy}-\sigma_{zzz}),\\
C_Y ={}& -\frac{1}{2}C^2(\sigma_{yyz}+\sigma_{yzy}) + \pi C(\sigma_{zyy}+\sigma_{zzz}).
\end{aligned} \tag{4}$$

The experimental results in Figs. 3(c) and 3(d) are in great agreement with Eq. (3). This further proves that the primary THz emission mechanism of VG SnS is shift current.

In microscopic view, the shift current is caused by the charge center "shift" when the carriers are excited from the valence band to the conduction band after absorbing incident photons. Such shift is driven by the coherent evolution of the electron and hole wave functions. Thus, the shift current not only requires broken inversion symmetry but also relates to the degree of asymmetry of the delocalized electronic states along the current direction [7,65]. The microscopic shift current response is given by $J_{\text{shift}}^a(\omega) = \sigma^{abc}E_bE_c$, where the second-order response function $\sigma^{abc}$ under the linearly polarized excitation is described as [66]

$$\sigma^{abc}(\omega) = -\frac{\pi e^3}{\hbar^2}\int\frac{d\mathbf{k}}{8\pi^3}\sum_{n,m} f_{nm}R_{nm}^a\left|r_{nm}^b\right|^2 \times \delta(\omega_{mn}-\omega). \tag{5}$$

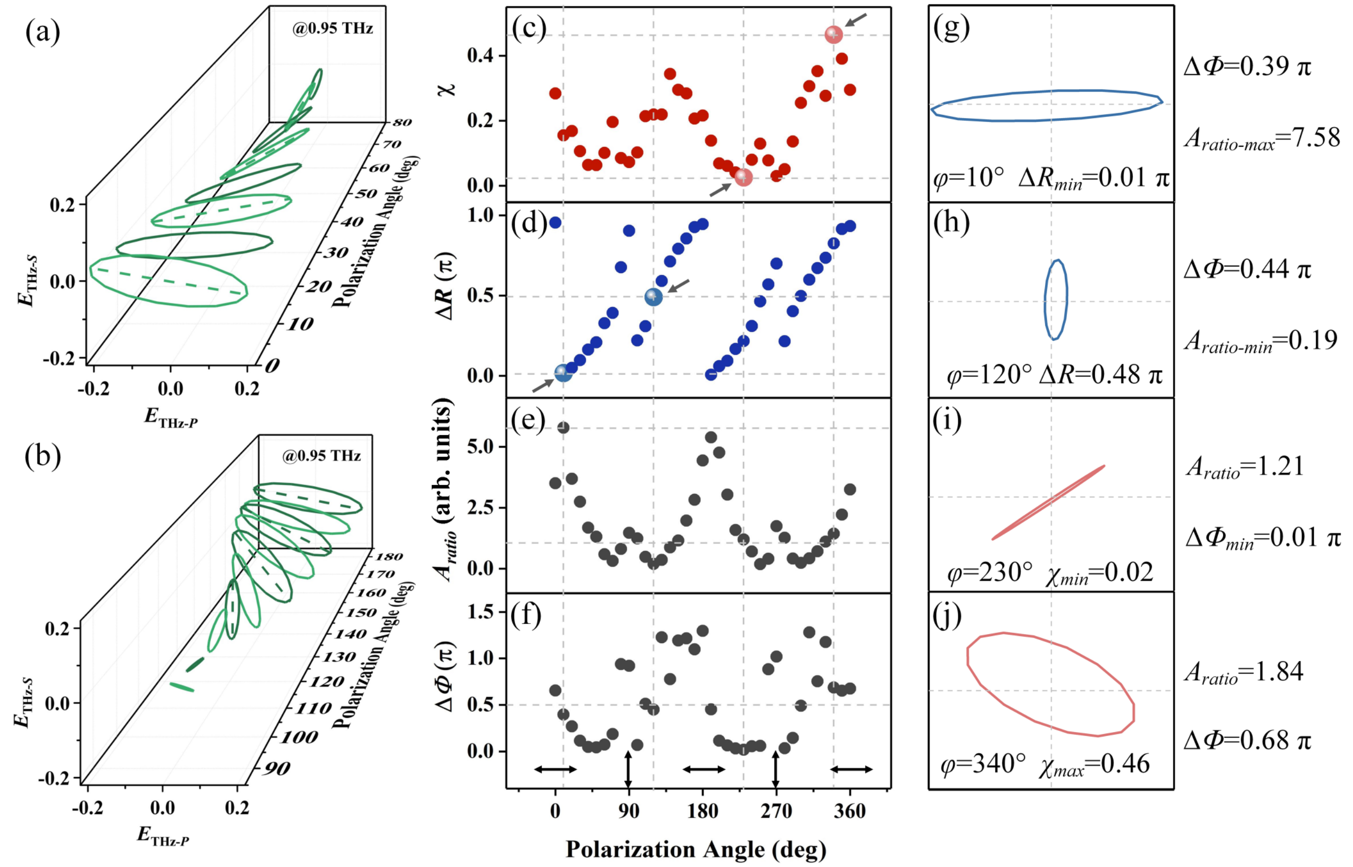

FIG. 6. The polarization ellipse of the THz emission with the pump light polarization angle $\varphi$ at (a) 0°–80° and (b) 90°–180°. (c) The ellipticity $\chi$ and (d) orientation angle $\Delta R$ of the THz polarization ellipses, as well as (e) the amplitude ratio $A_{ratio}$ and (f) phase difference $\Delta\Phi$ of $E_{\text{THz-}P}$ and $E_{\text{THz-}S}$ components with respect to the pump light polarization angle $\varphi$. (g)–(j) The THz polarization ellipses at $\varphi = 10°$, 120°, 230°, and 340°, respectively.

Herein, $f_{nm} = f_n - f_m$ represents Fermi-Dirac distribution, $r^b_{nm}$ are velocity matrix elements that correlate the linear absorption coefficient and the shift current, and $R^a_{nm}$ is a shift vector representing the position change of an electron when it absorbs a photon. Therefore, large velocity matrix elements $r^b_{nm}$ and shift vector $R^a_{nm}$ are essential factors that induce a robust shift current response in this microscopic frame. Interestingly, SnS and other monochalcogenides have a large shift vector and linear absorption in the visible range from the first-principles calculations [7]. Based on the theoretical model, various design strategies are expected to enhance the velocity matrix elements and shift vector [3,67], such as the internal manipulation including atom substitution, doping, and vacancy introduction as well as the external manipulation such as strain engineering and external electric field.

### E. Polarization state of the emitted THz wave

The shift current induced THz wave emission strongly depends on the polarization angle $\varphi$ of the excitation light according to Eq. (3) and Figs. 3(a) and 3(b). Can the trajectory of the THz polarization state also be modulated by the pump light polarization angle? To address this interesting question, we have portrayed the reconstructed $E_{\text{THz-}P}$ and $E_{\text{THz-}S}$ components based on $E(t) = E_{\text{THz-}P}(t)\hat{e}_x + E_{\text{THz-}S}(t)\hat{e}_y$ [27] at fixed 0.95 THz. As shown in Figs. 6(a) and 6(b), as the pump light polarization angle $\varphi$ is increased from 0° to 180°, the reconstructed ellipses of the THz waveforms exhibit different magnitudes and the major axis of the ellipse (dashed line in the ellipse) also rotates counterclockwise. Due to the weak $E_{\text{THz-}S}$ component at $\varphi = 90°$, a sudden change appears in the major axis of the THz polarization ellipse, but it still follows the overall trend of the counterclockwise rotation. In order to quantitatively analyze the polarization state of the THz radiation, we have extracted the ellipticity and orientation angle of the ellipses with respect to the pump light polarization angle, as shown in Figs. 6(c) and 6(d). The ellipticity $\chi$ is expressed as $\chi = b/a$, where $a$ and $b$ are the major and minor axis of the reconstructed polarization ellipses, respectively. The orientation angle $\Delta R$ is defined as the angle between the $x$ axis and the major axis of the ellipse. The minimum $\chi$ presents near the $s$ polarization ($\varphi = 90°$ and 270°), which approaches a linear polarization state, while the maximum $\chi$ of 0.46 locates at $\varphi = 340°$ near the $p$ polarization, corresponding to an elliptical polarization state. As such, the ellipticity $\chi$ presents twofold rotational symmetry with respect to the pump light polarization angle. This twofold rotational symmetry also occurs on the orientation angle $\Delta R$ when $\varphi$ increases from 0° to 360°, as shown in Fig. 6(d). On the contrary, the THz polarization ellipses are consistent at different azimuthal angles of VG

SnS (Appendix C), as the shift current response is independent of the azimuthal angle [Figs. 3(e) and 3(f)].

Since the THz polarization ellipses are composed of the $E_{\text{THz-}P}$ and $E_{\text{THz-}S}$ components, the $\chi$ and $\Delta R$ directly depend on the amplitude and phase of the THz components. Herein, the amplitude ratio of the THz components $A_{\text{ratio}} = A(E_{\text{THz-}P})/A(E_{\text{THz-}S})$ and the phase difference between the two components $\Delta\Phi = \Phi(E_{\text{THz-}P}) - \Phi(E_{\text{THz-}S})$ are shown in Figs. 6(e) and 6(f), respectively. Both the amplitude ratio $A_{\text{ratio}}$ and the phase difference $\Delta\Phi$ present twofold rotational symmetry with respect to the pump light polarization angle $\varphi$, which are in accordance with the ellipticity $\chi$ and the orientation angle $\Delta R$. In particular, when the phase difference $\Delta\Phi$ is in the region of $[0, \pi/2]$ and $[\pi/2, \pi]$, the major axis of the THz polarization ellipse locates at the I-III quadrant and the II-IV quadrant, respectively. In a certain quadrant, taking the ellipses at $\varphi = 10^\circ$ and $\varphi = 120^\circ$ as examples, the phase difference $\Delta\Phi$ at $\varphi = 10^\circ$ is close to that at $\varphi = 120^\circ$, but the orientation angle $\Delta R$ has different values. As shown in Figs. 6(g) and 6(h), when the amplitude ratio $A_{\text{ratio}}$ has a maximum value of 7.58 at $\varphi = 10^\circ$, the major axis of the ellipse approaches a horizontal direction, corresponding to the $\Delta R$ minimum of $0.01\pi$. On the contrary, when the amplitude of $E_{\text{THz-}P}$ is much smaller than that of $E_{\text{THz-}S}$ (with the minimum $A_{\text{ratio}}$ of 0.19) at $\varphi = 120^\circ$, the major axis of the ellipse approaches a vertical direction, then the $\Delta R$ value is close to $\pi/2$. Therefore, the orientation angle value is mainly determined by the THz amplitude ratio $A_{\text{ratio}}$ in a certain quadrant. As for the ellipticity $\chi$, the phase difference $\Delta\Phi$ is the key factor. As presented in Figs. 6(i) and 6(j), although the amplitude ratio $A_{\text{ratio}}$ has similar values at $\varphi = 230^\circ$ and $\varphi = 340^\circ$, the corresponding phase differences of $\Delta\Phi_{\min} = 0.01\pi$ and $\Delta\Phi = 0.68\pi$ result in ellipticity minimum $\chi_{\min} \sim 0.02$ and maximum $\chi_{\max} \sim 0.46$, respectively. Thus, when $\Delta\Phi$ approaches 0 or $\pi$, the THz wave emission is approximately linearly polarized, and $\chi$ approaches zero. When $\Delta\Phi$ is in the range of $(0, \pi)$, the THz polarization state is elliptical and the ellipticity $\chi$ is determined simultaneously by the amplitude ratio $A_{\text{ratio}}$ and the phase difference $\Delta\Phi$.

Considering the morphology of the VG SnS nanosheets, the amplitude ratio $A$ and phase difference $\Delta\Phi$ between the $E_{\text{THz-}P}$ and $E_{\text{THz-}S}$ components are primarily caused by the shift current component $J_Z$. Due to the spontaneous polarization $P_S^Z$, the photogenerated carriers are accelerated, and the shift current is improved along the $J_Z$ direction, which leads to a faster photocurrent response than $J_X$ and $J_Y$. According to the coordinates in Fig. 2(b), $J_Z$ only contributes to the $E_{\text{THz-}P}$ component, thereby resulting in amplitude differences and phase differences between the $E_{\text{THz-}P}$ and $E_{\text{THz-}S}$ components. For instance, $J_Z$ has a large value at $\varphi = 0^\circ$, which results in a phase difference between $E_{\text{THz-}P}$ and $E_{\text{THz-}S}$ and the reconstructed THz polarization is elliptically polarized, while $J_Z$ is approximately zero at $\varphi = 230^\circ$; thus the reconstructed THz polarization is linearly polarized. In particular, since the shift current components have strong dependences on the pump light polarization angle from Eq. (2), the ellipticity $\chi$ and orientation angle $\Delta R$ of the THz polarization ellipse realize a large modulation depth of $\chi_{\text{MD}} = 89.7\%$ [$\chi_{\text{MD}} = (\chi_{\max} - \chi_{\min})/(\chi_{\max} + \chi_{\min})$] and $\Delta R_{\text{MD}} = 98.5\%$ [$\Delta R_{\text{MD}} = (\Delta R_{\max} - \Delta R_{\min})/(\Delta R_{\max} + \Delta R_{\min})$] via tuning the pump light polarization angle. Such significant modulation depths enable the ferroelectric SnS as an enlightening candidate with tunability and designability for polarized THz devices, which are building blocks for polarized THz spectroscopy and hold promising potential in biomolecule identification and chiral sensing applications.

## IV. CONCLUSION

In summary, we have observed tunable polarized THz wave emission from the vertically grown SnS. The THz emission mechanism is ascribed to the shift current according to the time-domain THz signals with respect to the pump light polarization angle, sample azimuthal angle, and pump fluence. Interestingly, due to the spontaneous polarization along the armchair direction of the SnS nanosheets, the carrier movements and the shift current are enhanced in this direction, which is reflected by the reversed polarity of the THz wave from opposite pump directions. Since the shift current in VG SnS is sensitive to the pump light polarization angle, the ellipticity and the orientation angle of the elliptical THz wave realize a modulation depth of 89.7% and 98.5%, respectively. Our work offers an alternative way to generate, probe, and manipulate the shift current of ferroelectric SnS, which not only unveils the physics between the spontaneous polarization and the shift current, but also presents the intriguing potential of SnS for polarized THz devices.

## ACKNOWLEDGMENTS

This work was supported by the National Natural Science Foundation of China (Grants No. 12074311, No. 12004310, No. 11974279, No. 12104368, and No. 62004162), the Natural Science Foundation of Shaanxi Province (Grant No. 2020JQ-567), and the Natural Science Foundation of the Education Department of Shaanxi Province (Grant No. 21JK10917).

## APPENDIX A: INCIDENT fs LASER AND EMITTED THz WAVE WITHIN THE VG SnS

The $E_{\text{THz-}P}$ ($E_{\text{THz-}S}$) component lies in (is perpendicular to) the incident laser plane and parallel to the $E_P$ ($E_S$). Herein,

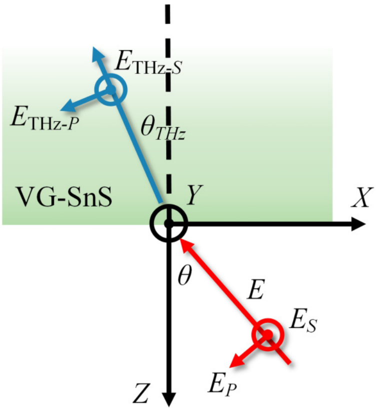

FIG. 7. Top view of the THz emission schematic under the fs laser excitation.

$E_{\text{THz-}P}$ is determined by $J_X$ and $J_Z$, and $E_{\text{THz-}S}$ is determined by $J_Y$. Both $E_{\text{THz-}P}$ and $E_{\text{THz-}S}$ components are obtained by the following angle relationship, as shown in Fig. 7.

## APPENDIX B: THz ELECTRIC FIELD DEPENDENCE ON THE PUMP LIGHT POLARIZATION ANGLE

The point group of SnS is $C_{2v}$ [7], and the nonlinear tensor element is shown as

$$\begin{bmatrix} 0 & 0 & 0 & 0 & 0 & xzx & xxz & 0 & 0 \\ 0 & 0 & 0 & yyz & yzy & 0 & 0 & 0 & 0 \\ zxx & zyy & zzz & 0 & 0 & 0 & 0 & 0 & 0 \end{bmatrix}. \tag{B1}$$

In the laboratory coordinate, concerning the pump polarization angle $\varphi$ and incident angle $\theta$, the electric field components of the pump light are given by

$$\begin{aligned} E_X &= E_P \cos\theta = -E\cos\varphi\cos\theta, \\ E_Y &= E_S = E\sin\varphi, \\ E_Z &= E_P \sin\theta = E\cos\varphi\sin\theta. \end{aligned} \tag{B2}$$

These electric field components can be transformed into the crystalline coordinate through a rotation matrix $R_X(\gamma)$ as shown in formula (B3).

$$\begin{aligned} \begin{pmatrix} E_x \\ E_y \\ E_z \end{pmatrix} = R_X(\gamma)\begin{pmatrix} E_X \\ E_Y \\ E_Z \end{pmatrix} &= \begin{pmatrix} \cos 90^\circ & 0 & \sin 90^\circ \\ 0 & 1 & 0 \\ -\sin 90^\circ & 0 & \cos 90^\circ \end{pmatrix}\begin{pmatrix} \cos\gamma & \sin\gamma & 0 \\ -\sin\gamma & \cos\gamma & 0 \\ 0 & 0 & 1 \end{pmatrix}\begin{pmatrix} -E\cos\varphi\cos\theta \\ E\sin\varphi \\ E\cos\varphi\sin\theta \end{pmatrix} \\ &= \begin{pmatrix} E\cos\varphi\sin\theta \\ E\cos\varphi\cos\theta\sin\gamma + E\sin\varphi\cos\gamma \\ E\cos\varphi\cos\theta\cos\gamma - E\sin\varphi\sin\gamma \end{pmatrix}. \end{aligned} \tag{B3}$$

Based on Eqs. (1) and (B3), the current density in the crystalline coordinate can be calculated by

$$\begin{aligned} J_x &= \sigma_{xzx}\frac{E_zE_x^* + E_xE_z^*}{2}I + \sigma_{xxz}\frac{E_xE_z^* + E_zE_x^*}{2}I, \quad J_y = \sigma_{yyz}\frac{E_yE_z^* + E_zE_y^*}{2}I + \sigma_{yzy}\frac{E_zE_y^* + E_yE_z^*}{2}I, \\ J_z &= \sigma_{zxx}\frac{E_xE_x^* + E_xE_x^*}{2}I + \sigma_{zyy}\frac{E_yE_y^* + E_yE_y^*}{2}I + \sigma_{zzz}\frac{E_zE_z^* + E_zE_z^*}{2}I. \end{aligned} \tag{B4}$$

Substituting Eq. (B3) into Eq. (B4), the current density in the crystalline coordinate system is described as

$$\begin{aligned} J_x &= (\sigma_{xzx} + \sigma_{xxz})\left(\tfrac{1}{2}E^2\sin 2\theta\cos\gamma\cos^2\varphi - \tfrac{1}{2}E^2\sin\theta\sin\gamma\sin 2\varphi\right)I, \\ J_y &= (\sigma_{yyz} + \sigma_{yzy})\left(\tfrac{1}{2}E^2\cos^2\theta\sin 2\gamma\cos^2\varphi - \tfrac{1}{2}E^2\cos\theta\sin^2\gamma\sin 2\varphi + \tfrac{1}{2}E^2\cos\theta\cos^2\gamma\sin 2\varphi - \tfrac{1}{2}E^2\sin 2\gamma\sin^2\varphi\right)I, \\ J_z &= \sigma_{zxx}E^2\sin^2\theta\cos^2\varphi I + \sigma_{zyy}\left(E^2\cos^2\theta\sin^2\gamma\cos^2\varphi + E^2\cos^2\gamma\sin^2\varphi + \tfrac{1}{2}E^2\cos\theta\sin 2\gamma\sin 2\varphi\right)I \\ &\quad + \sigma_{zzz}\left(E^2\cos^2\theta\cos^2\gamma\cos^2\varphi + E^2\sin^2\gamma\sin^2\varphi - \tfrac{1}{2}E^2\sin 2\gamma\cos\theta\sin 2\varphi\right)I. \end{aligned} \tag{B5}$$

The current density in the laboratory coordinate system can be obtained via rotating the azimuthal angle $\gamma$ as

$$J_X = J_y\sin\gamma - J_z\cos\gamma, \quad J_Y = J_y\cos\gamma + J_z\sin\gamma, \quad J_Z = J_x. \tag{B6}$$

Then we can obtain the current density in the laboratory coordinate as shown in Eq. (2) or (B7).

$$\begin{aligned} J_X &= (\sigma_{yyz} + \sigma_{yzy})CE^2\left(\frac{1}{4}C\cos^2\varphi - \frac{1}{2}C\sin^2\varphi\right)I - \frac{1}{2}CE^2\sigma_{zxx}\cos^2\varphi I - \sigma_{zyy}CE^2\left(\frac{1}{2}\pi\cos^2\varphi + \pi\sin^2\varphi + \frac{\sqrt{2}}{4}C\sin 2\varphi\right)I \\ &\quad - \sigma_{zzz}CE^2\left(\frac{1}{2}\pi\cos^2\varphi + \pi\sin^2\varphi - \frac{\sqrt{2}}{4}C\sin 2\varphi\right)I, \\ J_Y &= (\sigma_{yyz} + \sigma_{yzy})CE^2\left(\frac{1}{4}C\cos^2\varphi - \frac{1}{2}C\sin^2\varphi\right)I + \frac{1}{2}CE^2\sigma_{zxx}\cos^2\varphi I + \sigma_{zyy}CE^2\left(\frac{1}{2}\pi\cos^2\varphi + \pi\sin^2\varphi + \frac{\sqrt{2}}{4}C\sin 2\varphi\right)I \\ &\quad + \sigma_{zzz}CE^2\left(\frac{1}{2}\pi\cos^2\varphi + \pi\sin^2\varphi - \frac{\sqrt{2}}{4}C\sin 2\varphi\right)I, \\ J_Z &= (\sigma_{xzx} + \sigma_{xxz})E^2\left(\frac{1}{2}C\cos^2\varphi - \frac{\sqrt{2}}{4}C\sin 2\varphi\right)I. \end{aligned} \tag{B7}$$

Finally, the dependence between THz electric field $E_{\text{THz}}$ and pump light polarization angle $\varphi$ is obtained utilizing $E_{\text{THz}-P} \propto -\cos\theta_{\text{THz}}(\partial J_X/\partial t) + \sin\theta_{\text{THz}}(\partial J_Z/\partial t)$ and $E_{\text{THz}-S} \propto \partial J_Y/\partial t$, as shown in Eqs. (3) and (4).

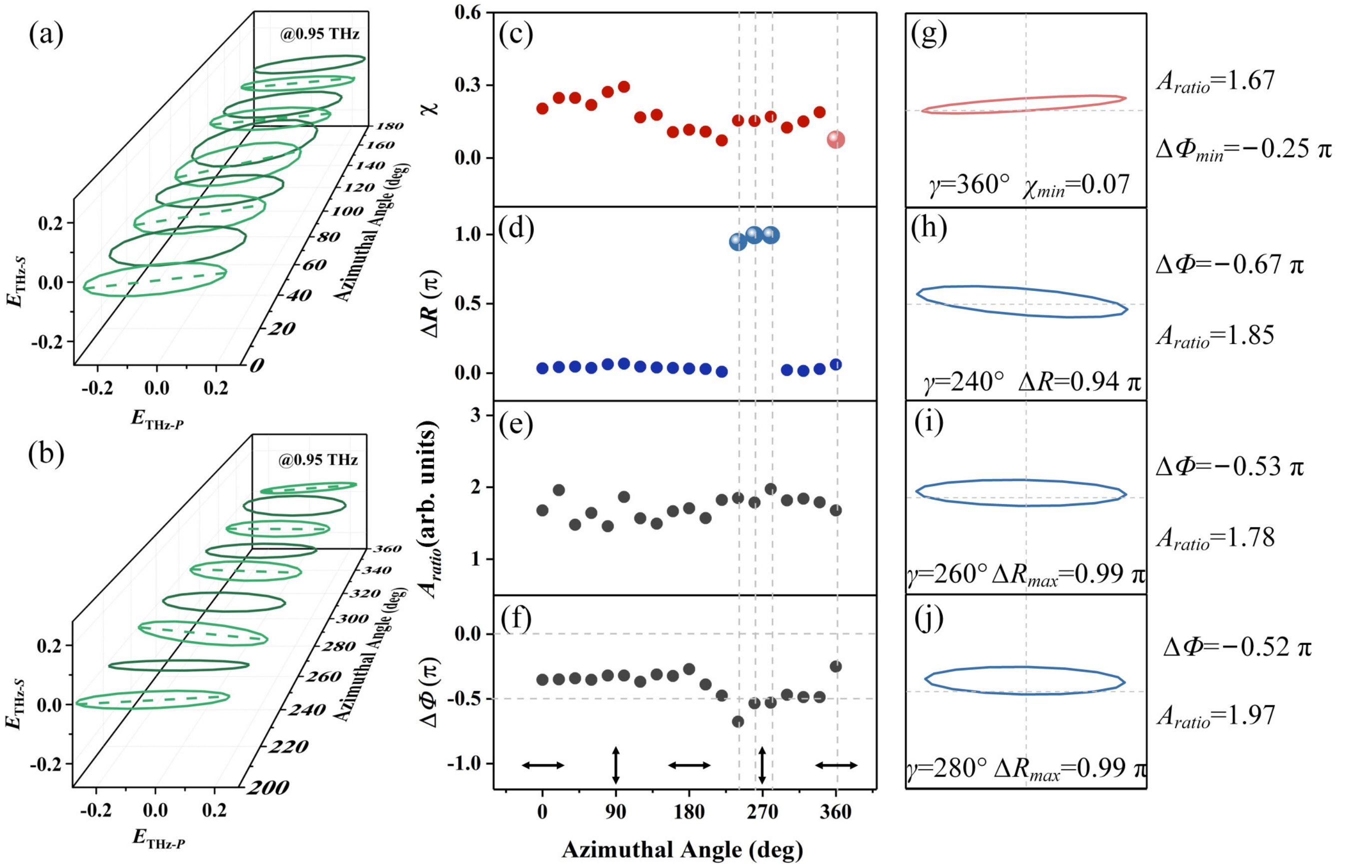

FIG. 8. The polarization ellipses of the THz wave emission with the azimuthal angle $\gamma$ at (a) 0°–180° and (b) 200°–360°. (c) The ellipticity $\chi$ and (d) orientation angle $\Delta R$ of the THz polarization ellipses, as well as (e) the amplitude ratio $A_{\mathrm{ratio}}$ and (f) phase difference $\Delta\Phi$ of $E_{\mathrm{THz}\text{-}P}$ and $E_{\mathrm{THz}\text{-}S}$ components with respect to the azimuthal angle $\gamma$. (g)–(j) The THz polarization ellipses at $\gamma = 240°$, 260°, 280°, and 360°, respectively.

## APPENDIX C: POLARIZATION STATE OF THE EMITTED THz WAVE WITH DIFFERENT AZIMUTHAL ANGLES

In contrast to the THz polarization ellipse dependence on the pump light polarization angle, the THz polarization ellipses are almost identical with the azimuthal angle changing from 0° to 360°. As given in Figs. 8(a) and 8(b), this group of elliptical trajectories exhibits the approximate ellipticity $\chi$ and similar orientation angle $\Delta R$. It can be seen from the reconstructed trajectory that the emitted THz polarization state is elliptical regardless of the azimuthal angle value. Meanwhile, the ellipticity $\chi$, orientation angle $\Delta R$, amplitude ratio $A_{\mathrm{ratio}}$, and phase difference $\Delta\Phi$ with respect to the azimuthal angle are shown in Figs. 8(c)–8(f), which verify that the ellipticity $\chi$ and orientation angle $\Delta R$ are determined by the phase difference $\Delta\Phi$ and amplitude ratio $A_{\mathrm{ratio}}$, respectively. The THz polarization ellipse at $\gamma = 360°$ has the minimum ellipticity $\chi$, which is caused by the minimum phase difference $\Delta\Phi$ as shown in Fig. 8(g). The orientation angle $\Delta R$ at $\gamma = 240°$, 260°, and 280° (approaching $\pi$) are much larger than that at other azimuthal angles (approaching zero) since the major axis of the ellipse locates at the II-IV quadrant [Figs. 8(h) and 8(i)].

[1] X. Mu, Y. Pan, and J. Zhou, Pure bulk orbital and spin photocurrent in two-dimensional ferroelectric materials, npj Comput. Mater. **7**, 61 (2021).

[2] S. V. Zhukovsky, V. E. Babicheva, A. B. Evlyukhin, I. E. Protsenko, A. V. Lavrinenko, and A. V. Uskov, Giant Photogalvanic Effect in Noncentrosymmetric Plasmonic Nanoparticles, Phys. Rev. X **4**, 031038 (2014).

[3] L. Z. Tan, F. Zheng, S. M. Young, F. Wang, S. Liu, and A. M. Rappe, Shift current bulk photovoltaic effect in polar materials—hybrid and oxide perovskites and beyond, npj Comput. Mater. **2**, 16026 (2016).

[4] R. Fei, L. Z. Tan, and A. M. Rappe, Shift-current bulk photovoltaic effect influenced by quasiparticle and exciton, Phys. Rev. B **101**, 045104 (2020).

[5] K. T. Butler, J. M. Frost, and A. Walsh, Ferroelectric materials for solar energy conversion: Photoferroics revisited, Energy Environ. Sci. **8**, 838 (2015).

[6] R. Fei, W. Kang, and L. Yang, Ferroelectricity and Phase Transitions in Monolayer Group-IV Monochalcogenides, Phys. Rev. Lett. **117**, 097601 (2016).

[7] T. Rangel, B. M. Fregoso, B. S. Mendoza, T. Morimoto, J. E. Moore, and J. B. Neaton, Large Bulk Photo-

voltaic Effect and Spontaneous Polarization of Single-Layer Monochalcogenides, Phys. Rev. Lett. **119**, 067402 (2017).

[8] C. He, J. Zhu, Y. H. Zhao, C. Liu, and B. Fu, Unconventional inner-TL electric polarization in TL-LaOBiS$_2$ with ultrahigh carrier mobility, Nanoscale **11**, 18436 (2019).

[9] L. Xu, M. Yang, S. J. Wang, and Y. P. Feng, Electronic and optical properties of the monolayer group-IV monochalcogenides $MX$ ($M$ = Ge, Sn; $X$ = S, Se, Te), Phys. Rev. B **95**, 235434 (2017).

[10] H. Wang and X. Qian, Two-dimensional multiferroics in monolayer group IV monochalcogenides, 2D Mater. **4**, 015042 (2017).

[11] R. Fei, W. Li, J. Li, and L. Yang, Giant piezoelectricity of monolayer group IV monochalcogenides: SnSe, SnS, GeSe, and GeS, Appl. Phys. Lett. **107**, 173104 (2015).

[12] M. Wu and X. C. Zeng, Intrinsic ferroelasticity and/or multiferroicity in two-dimensional phosphorene and phosphorene analogues, Nano Lett. **16**, 3236 (2016).

[13] P. D. Antunez, J. J. Buckley, and R. L. Brutchey, Tin and germanium monochalcogenide IV-VI semiconductor nanocrystals for use in solar cells, Nanoscale **3**, 2399 (2011).

[14] N. Higashitarumizu, H. Kawamoto, C. J. Lee, B. H. Lin, F. H. Chu, I. Yonemori, T. Nishimura, K. Wakabayashi, W. H. Chang, and K. Nagashio, Purely in-plane ferroelectricity in monolayer SnS at room temperature, Nat. Commun. **11**, 2428 (2020).

[15] G. Liu, Y. Li, B. Li, H. Tian, C. Fan, Y. Zhang, Z. Hua, M. Wang, H. Zheng, and E. Li, High-performance photodetectors based on two-dimensional tin(II) sulfide (SnS) nanoflakes, J. Mater. Chem. C **6**, 10036 (2018).

[16] A. Nalin Mehta, H. Zhang, A. Dabral, O. Richard, P. Favia, H. Bender, A. Delabie, M. Caymax, M. Houssa, G. Pourtois, and W. Vandervorst, Structural characterization of SnS crystals formed by chemical vapour deposition, J. Microsc. **268**, 276 (2017).

[17] T. J. Whittles, L. A. Burton, J. M. Skelton, A. Walsh, T. D. Veal, and V. R. Dhanak, Band alignments, valence bands, and core levels in the tin sulfides SnS, SnS$_2$, and Sn$_2$S$_3$: Experiment and theory, Chem. Mater. **28**, 3718 (2016).

[18] C. Xin, J. Zheng, Y. Su, S. Li, B. Zhang, Y. Feng, and F. Pan, Few-layer tin sulfide: A new black-phosphorus-analogue 2D material with a sizeable band gap, odd–even quantum confinement effect, and high carrier mobility, J. Phys. Chem. C **120**, 22663 (2016).

[19] Y. Bao, P. Song, Y. Liu, Z. Chen, M. Zhu, I. Abdelwahab, J. Su, W. Fu, X. Chi, W. Yu, W. Liu, X. Zhao, Q. H. Xu, M. Yang, and K. P. Loh, Gate-tunable in-plane ferroelectricity in few-layer SnS, Nano Lett. **19**, 5109 (2019).

[20] M. Alexe and D. Hesse, Tip-enhanced photovoltaic effects in bismuth ferrite, Nat. Commun. **2**, 256 (2011).

[21] J. Ding, M. Chen, J. Qiu, and N. Yuan, Photovoltaic properties of ferroelectric solar cells based on polycrystalline BiFeO$_3$ films sputtered on indium tin oxide substrates, Sci. China Phys. Mech. Astron. **58**, 1 (2015).

[22] Y. Pan and J. Zhou, Toggling Valley-Spin Locking and Nonlinear Optical Properties of Single-Element Multiferroic Monolayers via Light, Phys. Rev. Appl. **14**, 014024 (2020).

[23] L. Zhu, Y. Huang, Z. Yao, B. Quan, L. Zhang, J. Li, C. Gu, X. Xu, and Z. Ren, Enhanced polarization-sensitive terahertz emission from vertically grown graphene by a dynamical photon drag effect, Nanoscale **9**, 10301 (2017).

[24] L. Zhang, Y. Huang, Q. Zhao, L. Zhu, Z. Yao, Y. Zhou, W. Du, and X. Xu, Terahertz surface emission of $d$-band electrons from a layered tungsten disulfide crystal by the surface field, Phys. Rev. B **96**, 155202 (2017).

[25] Z. Lei, Y. Huang, Z. Fan, W. Du, C. He, H. Wang, Y. Jin, and X. Xu, Terahertz emission from in-plane and out-of-plane dipoles in layered SnS$_2$ crystal, Appl. Phys. Lett. **116**, 161901 (2020).

[26] Y. Huang, Z. Yao, C. He, L. Zhu, L. Zhang, J. Bai, and X. Xu, Terahertz surface and interface emission spectroscopy for advanced materials, J. Phys.: Condens. Matter **31**, 153001 (2019).

[27] J. Chang, H. Wang, Z. Lei, W. Du, Y. Huang, Y. Zhou, L. Zhu, and X. Xu, Coherent elliptically polarized terahertz wave generation in WSe$_2$ by linearly polarized femtosecond laser excitation, J. Phys. Chem. Lett. **12**, 10068 (2021).

[28] L. Braun, G. Mussler, A. Hruban, M. Konczykowski, T. Schumann, M. Wolf, M. Munzenberg, L. Perfetti, and T. Kampfrath, Ultrafast photocurrents at the surface of the three-dimensional topological insulator Bi$_2$Se$_3$, Nat. Commun. **7**, 13259 (2016).

[29] M. Tong, Y. Hu, W. He, X. L. Yu, S. Hu, X. Cheng, and T. Jiang, Ultraefficient terahertz emission mediated by shift-current photovoltaic effect in layered gallium telluride, ACS Nano **15**, 17565 (2021).

[30] K. Kushnir, Y. Qin, Y. Shen, G. Li, B. M. Fregoso, S. Tongay, and L. V. Titova, Ultrafast zero-bias surface photocurrent in germanium selenide: Promise for terahertz devices and photovoltaics, ACS Appl. Mater. Interfaces **11**, 5492 (2019).

[31] K. Kushnir, M. Wang, P. D. Fitzgerald, K. J. Koski, and L. V. Titova, Ultrafast zero-bias photocurrent in GeS nanosheets: Promise for photovoltaics, ACS Energy Lett. **2**, 1429 (2017).

[32] W. Dong, C. Lu, M. Luo, Y. Liu, T. Han, Y. Ge, X. Xue, Y. Zhou, and X. Xu, Enhanced UV-Vis photodetector performance by optimizing interfacial charge transportation in the heterostructure by SnS and SnSe$_2$, J. Colloid Interface Sci. **621**, 374 (2022).

[33] H. Huang, B. Jiang, X. Zou, X. Zhao, and L. Liao, Black phosphorus electronics, Sci. Bull. **64**, 1067 (2019).

[34] X. Wang and S. Lan, Optical properties of black phosphorus, Adv. Opt. Photonics **8**, 618 (2016).

[35] H. Choi, J. Lee, S. Shin, J. Lee, S. Lee, H. Park, S. Kwon, N. Lee, M. Bang, S. B. Lee, and H. Jeon, Fabrication of high crystalline SnS and SnS$_2$ thin films, and their switching device characteristics, Nanotechnology **29**, 215201 (2018).

[36] J. R. Brent, D. J. Lewis, T. Lorenz, E. A. Lewis, N. Savjani, S. J. Haigh, G. Seifert, B. Derby, and P. O'Brien, Tin(II) sulfide (SnS) nanosheets by liquid-phase exfoliation of herzenbergite: IV-VI main group two-dimensional atomic crystals, J. Am. Chem. Soc. **137**, 12689 (2015).

[37] M. Li, Y. Wu, T. Li, Y. Chen, H. Ding, Y. Lin, N. Pan, and X. Wang, Revealing anisotropy and thickness dependence of Raman spectra for SnS flakes, RSC Adv. **7**, 48759 (2017).

[38] J. H. Ahn, M. J. Lee, H. Heo, J. H. Sung, K. Kim, H. Hwang, and M. H. Jo, Deterministic two-dimensional polymorphism growth of hexagonal $n$-type SnS$_2$ and orthorhombic $p$-type SnS crystals, Nano Lett. **15**, 3703 (2015).

[39] M. Patel, J. Kim, and Y. K. Kim, Growth of large-area SnS films with oriented 2D SnS layers for energy-efficient

broadband optoelectronics, Adv. Funct. Mater. **28**, 1804737 (2018).

[40] R. E. Abutbul, E. Segev, L. Zeiri, V. Ezersky, G. Makov, and Y. Golan, Synthesis and properties of nanocrystalline $\pi$-SnS–a new cubic phase of tin sulphide, RSC Adv. **6**, 5848 (2016).

[41] Q. Wu and X. C. Zhang, Free-space electro-optics sampling of mid-infrared pulses, Appl. Phys. Lett. **71**, 1285 (1997).

[42] S. V. Popov, Y. P. Svirko, and N. I. Zheludev, *Susceptibility Tensors for Nonlinear Optics* (Taylor & Francis, Milton Park, UK, 1995).

[43] Y. Huang, L. Zhu, Q. Zhao, Y. Guo, Z. Ren, J. Bai, and X. Xu, Surface optical rectification from layered $MoS_2$ crystal by THz time-domain surface emission spectroscopy, ACS Appl. Mater. Interfaces **9**, 4956 (2017).

[44] A. Rice, Y. Jin, X. F. Ma, X. C. Zhang, D. Bliss, J. Larkin, and M. Alexander, Terahertz optical rectification from $\langle 110\rangle$ zinc-blende crystals, Appl. Phys. Lett. **64**, 1324 (1994).

[45] M. B. Johnston, D. M. Whittaker, A. Corchia, A. G. Davies, and E. H. Linfield, Theory of magnetic-field enhancement of surface-field terahertz emission, J. Appl. Phys. **91**, 2104 (2002).

[46] E. Estacio, H. Sumikura, H. Murakami, M. Tani, N. Sarukura, M. Hangyo, C. Ponseca, R. Pobre, R. Quiroga, and S. Ono, Magnetic-field-induced fourfold azimuthal angle dependence in the terahertz radiation power of (100) InAs, Appl. Phys. Lett. **90**, 151915 (2007).

[47] K. Takahashi, T. Kanno, A. Sakai, H. Tamaki, H. Kusada, and Y. Yamada, Terahertz radiation via ultrafast manipulation of thermoelectric conversion in thermoelectric thin films, Adv. Opt. Mater. **2**, 428 (2014).

[48] G. Ramakrishnan, R. Chakkittakandy, and P. Planken, Terahertz generation from graphite, Opt. Express **17**, 16092 (2009).

[49] X. L. Xu, P. Parkinson, K. C. Chuang, M. B. Johnston, R. J. Nicholas, and L. M. Herz, Dynamic terahertz polarization in single-walled carbon nanotubes, Phys. Rev. B **82**, 085441 (2010).

[50] H. Wang, J. Chang, Y. Huang, Z. Lei, W. Du, Y. Zhou, Y.E., and X. Xu, Large in-plane anisotropic terahertz emission induced by asymmetric polarization in low-symmetric $PdSe_2$, ACS Appl. Mater. Interfaces **13**, 54543 (2021).

[51] S. Huang, W. Li, L. Zhu, M. He, Z. Yao, Y. Zhou, X. Xu, Z. Ren, and J. Bai, Terahertz emission from vertically aligned multi-wall carbon nanotubes and their composites by optical excitation, Carbon **132**, 335 (2018).

[52] Z. Fan, M. Xu, Y. Huang, Z. Lei, L. Zheng, Z. Zhang, W. Zhao, Y. Zhou, X. Wang, X. Xu, and Z. Liu, Terahertz surface emission from $MoSe_2$ at the monolayer limit, ACS Appl. Mater. Interfaces **12**, 48161 (2020).

[53] H. Plank, J. Pernul, S. Gebert, S. N. Danilov, J. König-Otto, S. Winnerl, M. Lanius, J. Kampmeier, G. Mussler, I. Aguilera, D. Grützmacher, and S. D. Ganichev, Infrared/terahertz spectra of the photogalvanic effect in (Bi,Sb)Te based three-dimensional topological insulators, Phys. Rev. Mater. **2**, 024202 (2018).

[54] Y. Hirai, N. Yoshikawa, H. Hirose, M. Kawaguchi, M. Hayashi, and R. Shimano, Terahertz Emission from Bismuth Thin Films Induced by Excitation with Circularly Polarized Light, Phys. Rev. Appl. **14**, 064015 (2020).

[55] L. Zhu, Z. Yao, Y. Huang, C. He, B. Quan, J. Li, C. Gu, X. Xu, and Z. Ren, Circular-Photon-Drag-Effect-Induced Elliptically Polarized Terahertz Emission from Vertically Grown Graphene, Phys. Rev. Appl. **12**, 044063 (2019).

[56] P. A. Obraztsov, N. Kanda, K. Konishi, M. Kuwata-Gonokami, S. V. Garnov, A. N. Obraztsov, and Y. P. Svirko, Photon-drag-induced terahertz emission from graphene, Phys. Rev. B **90**, 241416(R) (2014).

[57] H. Kawamoto, N. Higashitarumizu, N. Nagamura, M. Nakamura, K. Shimamura, N. Ohashi, and K. Nagashio, Micrometer-scale monolayer SnS growth by physical vapor deposition, Nanoscale **12**, 23274 (2020).

[58] H.-Y. Song and J.-T. Lü, Density functional theory study of inter-layer coupling in bulk tin selenide, Chem. Phys. Lett. **695**, 200 (2018).

[59] Y. Zhou, D. Wu, Y. Zhu, Y. Cho, Q. He, X. Yang, K. Herrera, Z. Chu, Y. Han, M. C. Downer, H. Peng, and K. Lai, Out-of-plane piezoelectricity and ferroelectricity in layered alpha-$In_2Se_3$ nanoflakes, Nano Lett. **17**, 5508 (2017).

[60] W. Ji, K. Yao, and Y. C. Liang, Bulk photovoltaic effect at visible wavelength in epitaxial ferroelectric $BiFeO_3$ thin films, Adv. Mater. **22**, 1763 (2010).

[61] L. Pintilie, V. Stancu, E. Vasile, and I. Pintilie, About the complex relation between short-circuit photocurrent, imprint and polarization in ferroelectric thin films, J. Appl. Phys. **107**, 114111 (2010).

[62] L. Pintilie, I. Vrejoiu, G. L. Rhun, and M. Alexe, Short-circuit photocurrent in epitaxial lead zirconate-titanate thin films, J. Appl. Phys. **101**, 064109 (2007).

[63] M. M. Glazov and S. D. Ganichev, High frequency electric field induced nonlinear effects in graphene, Phys. Rep. **535**, 101 (2014).

[64] W. Du, Z. Yao, L. Zhu, Y. Huang, Z. Lei, F. Xi, Y. Jin, and X. Xu, Photodoping of graphene/silicon van der Waals heterostructure observed by terahertz emission spectroscopy, Appl. Phys. Lett. **117**, 081106 (2020).

[65] S. M. Young and A. M. Rappe, First Principles Calculation of the Shift Current Photovoltaic Effect in Ferroelectrics, Phys. Rev. Lett. **109**, 116601 (2012).

[66] J. E. Sipe and A. I. Shkrebtii, Second-order optical response in semiconductors, Phys. Rev. B **61**, 5337 (2000).

[67] A. M. Cook, B. M. Fregoso, F. de Juan, S. Coh, and J. E. Moore, Design principles for shift current photovoltaics, Nat. Commun. **8**, 14176 (2017).